

# Relativistic Coulomb Screening in Pulsational Pair Instability Supernovae

M.A. Famiano<sup>1-3,\*</sup>, K. Mori<sup>4,\*\*</sup>, A.B. Balantekin<sup>2,5,\*\*\*</sup>, T. Kajino<sup>2,6,7,\*\*\*\*</sup>, M.  
Kusakabe<sup>7,†</sup>, and G. Mathews<sup>3,8,‡</sup>

<sup>1</sup> Department of Physics, Western Michigan University, Kalamazoo, MI 49008 USA

<sup>2</sup> National Astronomical Observatory of Japan, 2-21-1 Osawa, Mitaka, Tokyo 181-8588 Japan

<sup>3</sup> Joint Institute for Nuclear Astrophysics - Center for the Evolution of the Elements, USA

<sup>4</sup> Research Institute of Stellar Explosive Phenomena, Fukuoka University, 8-19-1 Nanakuma,  
Jonan-ku, Fukuoka-shi, Fukuoka 814-0180, Japan

<sup>5</sup> Department of Physics, University of Wisconsin-Madison, Madison, Wisconsin 53706 USA

<sup>6</sup> Graduate School of Science, The University of Tokyo, 7-3-1 Hongo, Bunkyo-ku, Tokyo, 113-  
0033 Japan

<sup>7</sup> School of Physics, Beihang University, 37 Xueyuan Road, Haidian-qu, Beijing 100083, China

<sup>8</sup> Center for Astrophysics, Department of Physics, University of Notre Dame, 225 Nieuwland  
Science Hall, Notre Dame, IN 46556, USA

Received XXXX; accepted XXXX

## ABSTRACT

*Context.* Pulsational pair-instability supernovae (PPISNe) and pair instability supernovae (PISNe) are the result of a thermonuclear runaway in the presence of a background electron-positron pair plasma. As such, their evolution and resultant black hole (BH) masses could possibly be affected by screening corrections due to the electron pair plasma.

*Aims.* Sensitivity of PISNe and PPISNe to relativistic weak screening has been explored.

*Methods.* In this paper a weak screening model that includes effects from relativistic pair production has been developed and applied at temperatures approaching and exceeding the threshold for pair production. This screening model replaces “classical” screening commonly used in astrophysics. Modifications to the weak screening electron Debye length are incorporated in a computationally tractable analytic form with.

\* Corresponding Author, e-mail: michael.famiano@wmich.edu

\*\* e-mail: kanji.mori@fukuoka-u.ac.jp

\*\*\* e-mail: baha@physics.wisc.edu

\*\*\*\* e-mail: kajino@buaa.edu.cn

† e-mail: kusakabe@buaa.edu.cn

‡ e-mail: gmathews@nd.edu

*Results.* In PPISNe the BH masses were found to increase somewhat at high temperatures, though this increase is small. The BH collapse is also found to occur at earlier times, and the pulsational morphology also changes. In addition to the resultant BH mass, the sensitivity to the screening model of the pulsational period, the pulse structure, the PPISN-to-PISN transition, and the shift in the BH mass gap has been analyzed. The dependence of the composition of the ejected mass was also examined.

**Key words.** instabilities – nuclear reactions, nucleosynthesis, abundances – plasmas – relativistic processes – stars: massive – supernovae: general

## 1. Introduction

Currently, there is considerable interest in the black hole mass gap (BHMg). That is, black hole masses in the range of  $\sim 50 - 120 M_{\odot}$  are not expected to exist (Woosley et al. 2007; Belczynski et al. 2016; Woosley 2017, 2019) because progenitor stars in this mass range are disrupted by pair-instability supernovae (PISNe) or pulsational pair-instability supernovae (PPISNe). The existence of this mass gap, however, has been brought into question by the observed LIGO/VIRGO gravitational wave event GW190521 (Abbott et al. 2020) from which two black holes of masses  $m_1 = 85^{+21}_{-14} M_{\odot}$  and  $m_2 = 66^{+17}_{-18} M_{\odot}$  were deduced. Since both of these merging black holes are well within the putative black-hole mass gap, a re-examination of the constraints on black-hole masses from the pair instability and PPISNe is warranted (e.g., Farmer et al. 2019; Marchant et al. 2019; Abbott et al. 2020; Croon et al. 2020; van Son et al. 2020; Woosley & Heger 2021). Indeed, the existence of the BHMg and the associated progenitor evolution is sensitive to a host of astrophysical parameters as noted in Farmer et al. (2019); Sakstein et al. (2020); Woosley & Heger (2021). In this paper we consider one additional sensitivity, i.e. the effects of relativistic screening of the thermonuclear reaction rates in the background associated pair plasma. Although, we find that the effects on the BHMg are small, we point out a number of interesting features of the evolution of the progenitors that depend upon the nature of the electron screening. In what follows we briefly summarize the physics of PISNe and PPISNe in §1.1. We describe a model for electron screening in a relativistic pair plasma in §1.2. The computations are described in §2, and results given in §3. §4 contains the conclusions of this work.

### 1.1. Pulsational Pair Instability Supernovae and Pair Instability Supernovae

PISNe are caused by the production of electron-positron pairs in the cores of massive ( $M_{ZAMS} \gtrsim 80 M_{\odot}$ ) stars at the end of their lifetimes (Leung et al. 2019). At temperatures  $\gtrsim 10^9$  K, electron pairs are produced by the thermal plasma, e.g. via  $\gamma + \gamma \Leftrightarrow e^- + e^+$ . As the photons are absorbed into pair production, the radiation pressure support of the core diminishes. Subsequently, the core contracts and the temperature rises. This leads to explosive thermonuclear oxygen burning. The

release of this thermonuclear energy can be comparable to the binding energy of the star and lead to substantial mass ejection.

The details of the explosion and associated nucleosynthesis, however, depend upon the mass and metallicity of the progenitor star. At low metallicity,  $Z \sim 10^{-3}$ , stars in the mass range of  $\sim 50 - 90 M_{\odot}$  can experience a sequence of contractions and explosions. This is referred to as a PPISN. Eventually, these stars can return to hydrostatic equilibrium and then collapse. However, the resultant black holes are significantly less massive than they would have been without the onset of the pair instability.

On the other hand, more massive progenitors with  $M \geq 90 M_{\odot}$  experience such violent explosions that no black-hole remnant remains. These have been dubbed as PISNe. The most massive black hole that can be formed before mass loss from the PPISN becomes significant defines the lower limit of the black hole mass gap. In the heaviest progenitors for which  $M \gtrsim 240 M_{\odot}$ , the pair instability is quenched because the interior temperatures are high enough to photodisintegrate heavy elements. This precludes the onset of runaway thermonuclear burning. The lightest black hole formed in this way [ $\sim 120 M_{\odot}$  after mass loss (Heger & Woosley 2002)] defines the upper edge of the black hole mass gap.

### 1.2. Coulomb Screening in Nuclear Reactions

Astrophysical reaction rates in stellar plasmas can be very sensitive to the tails of the Coulomb potentials between two reacting charged nuclei. This is because charged nuclei in astrophysical environments have center-of-mass energies  $\sim kT$  well below the height of the Coulomb barriers. For an environment at a certain temperature, the average thermonuclear reaction rates between charged particles are determined by integrating the energy-dependent cross section times the Maxwell-Boltzmann energy distribution for the reactants involved to obtain the average thermonuclear reaction rate (TRR),  $\langle \sigma v \rangle$  (Boyd 2008; Iliadis 2007). Resonances at specific energies are similarly determined with a term in the cross section which defines the resonance.

However, one must also account for “screening” between the two reacting, nuclei due to the background charges and (fully or partially) ionized nuclei. Coulomb screening results in a reduction in the effective Coulomb barrier between the two reacting nuclei and an increase in the WKB penetrability of the barrier, leading to an increase in the overall rate. This effect has been well studied and is incorporated into multiple existing astrophysics calculations and codes (Wu & Pálffy 2017; Liu 2016; Spitaleri et al. 2016; Kravchuk & Yakovlev 2014a,b; Potekhin & Chabrier 2013; Quarati & Scarfone 2007; Shaviv & Shaviv 2000; Adelberger et al. 1998; Shalybkov & Yakovlev 1987; Wang et al. 2011; Wallace et al. 1982; Itoh et al. 1977; Jancovici 1977; Graboske et al. 1973; Dewitt et al. 1973; Salpeter & van Horn 1969; Salpeter 1954).

When evaluating the effects of electron screening on the Coulomb potential, even a small shift in the potential can result in significant changes in the classical potential turning points, resulting in an increase in the reaction rate. For positively charged nuclei the overall reaction rates increase

because charges are re-distributed non-uniformly in the presence of the central nuclear potential. Despite the extensive development of nuclear screening effects on thermonuclear reaction rates, relativistic plasma effects have not yet been fully addressed. If the temperature is high enough, electron-positron pairs are created, and these add additional charged particles to the plasma. Recalling that any charge added to the plasma results in a net reduction in the Coulomb potential, pair production can have an additional effect on screening. In addition, if the plasma is magnetized, the electron-positron momentum distributions are quantized into Landau levels, further changing the overall energy distribution, resultant numbers of electrons and positrons, and the overall screening characteristics of the plasma (Famiano et al. 2020). Applying these effects to massive stars (Kozyreva et al. 2017; Woosley 2017; Spera & Mapelli 2017; Takahashi et al. 2018) or to neutrino cooling mechanisms (Itoh et al. 1996) is potentially very interesting.

For a hot, ionized plasma, the Coulomb potential between two reacting nuclei is reduced by the presence of background charges. Assuming charge neutrality, the electrostatic potential,  $\phi$  of a particle with charge  $Ze$  immersed in a set of background charge distributions is determined via the Poisson-Boltzmann equation:

$$\nabla^2 \phi(r) = -4\pi Ze^2 \delta(\mathbf{r}^3) - 4\pi \sum_{z \geq -1} z e n_z \exp\left[-\frac{Zze^2 \phi(r)}{kT}\right]. \quad (1)$$

Here, the summation in the last term is over all charges  $ze$  in the plasma having number density  $n_z$ . Note that this sum includes electrons, with  $z = -1$ . The results of this calculation are widely used in astrophysical calculations, despite the assumption of a classical (Boltzmann) energy distribution for all of the particles, given by the second term in the above equations. With this, evaluations of the electron degeneracy must be explicitly determined to obtain the electron number density and resulting energy distribution.

In the case of a hot, unmagnetized plasma, the energy distribution must be replaced with the corresponding distribution assuming Fermi-Dirac statistics. The Poisson-Boltzmann equation must be replaced with the equivalent equation assuming Fermi statistics and chemical potential,  $\mu$  (Famiano et al. 2016, 2020):

$$\begin{aligned} \nabla^2 \phi_r &= -4\pi Ze^2 \delta(\mathbf{r}^3) - 4\pi \sum_{z>0} z e n_z \exp\left[-\frac{Zze^2 \phi_r}{kT}\right] \\ &\quad - \frac{4e}{\pi} \int_0^\infty p^2 dp \left[ \frac{1}{\exp(E-\mu-e\phi_r)/T+1} - \frac{1}{\exp(E+\mu+e\phi_r)/T+1} \right]. \end{aligned} \quad (2)$$

Relativistic effects come from the high thermal energy. (Natural units are used:  $k = \hbar = c = 1$ .) This relationship can also be deduced from a solution to the Schwinger-Dyson equation for the photon propagator (Kapusta & Gale 2006). Here, the much heavier nuclei can be safely treated with Boltzmann statistics.

If the temperature is high enough, such that the average Coulomb energy between two interacting particles is much less than the thermal energy of the plasma,  $E_C/kT \ll 1$ , “weak screening” can apply. In such a plasma, the electrons are mostly non-degenerate. Equations 1 and 2 can be

expanded to first order in the potential. This expansion to  $O(\phi)$  is known as the Debye-Hückel approximation, and the usual  $1/r$  Coulomb potential takes on a Yukawa form,  $\phi(r) \propto e^{-r/\lambda_D}/r$  where the characteristic length  $\lambda_D$  is known as the Debye length. A similar Thomas-Fermi screening length can be derived using the density of states at the electron Fermi surface (Ichimaru 1993) with a screening length,  $\lambda_{TF} \propto \partial n / \partial \mu$ .

At the other extreme in the temperature-density relationship is “strong screening.” At high densities, the average distance between nuclei is small enough such that the average Coulomb energy is much larger than the thermal energy,  $E_C/kT \gg 1$ . Here, the linear approximation for Debye-Hückel or Thomas-Fermi screening is inadequate. Likewise, the electron chemical potential becomes larger and must be accounted for in Equation 2. In this regime, generally the “ion sphere” screening model is used, in which the potential is modified by the difference in Coulomb energy between the reactants and products of a reaction (Clayton 1983; Salpeter & van Horn 1969; Salpeter 1954).

Between weak and strong screening, where  $E_C \sim kT$ , there is still much work to be done, and computational methods can be tricky. While the electron degeneracy and Coulomb potentials can be numerically calculated (Graboske et al. 1973), in order to maintain computational efficiency, approximate methods are often adopted to treat screening in this region. Numerical fits and tables have also been used to determine reaction-rate enhancements due to screening. Other commonly-used tools rely on interpolation or averaging schemes to determine the screening enhancement in this region (Meyer & Adams 2007; Wallace et al. 1982; Salpeter & van Horn 1969; Paxton et al. 2011a).

Ultimately, the increase in nuclear reaction rates is expressed by the “screening enhancement factor” (SEF),  $f$  which relates the unscreened and screened rates,  $\langle \sigma v \rangle_{uns}$  and  $\langle \sigma v \rangle_{scr}$  respectively. In the Salpeter approximation (Salpeter 1954), the screened rate is then  $\langle \sigma v \rangle_{scr} = f \langle \sigma v \rangle_{uns}$ . This results from assuming that the shift in the screening potential is much less than the height of the Coulomb potential and can be treated to first order in the WKB approximation. The value of  $f$  is then expressed as  $f = e^H$  (Graboske et al. 1973; Jancovici 1977; Salpeter 1954; Salpeter & van Horn 1969; Wallace et al. 1982). The value of  $H$  is unitless and is determined based upon the screening model used (Sahoo & Das 2016; Kravchuk & Yakovlev 2014b; Itoh et al. 1977; Alastuey & Jancovici 1978; Dewitt et al. 1973; Quarati & Scarfone 2007). In the case of intermediate screening discussed briefly above,  $H_I$  commonly results from an interpolation between strong and weak screening or a type of geometric mean (Paxton et al. 2011a, 2015, 2018; Meyer & Adams 2007). For example, Wallace et al. (1982) sets  $H_I = H_S H_W / \sqrt{H_S^2 + H_W^2}$  while the MESA code (Paxton et al. 2011a, 2015, 2018) relies on a type of linear interpolation based upon the effective screening parameter discussed in §2.2.

In this paper, effects of the inclusion of Fermi-Dirac statistics in the electron screening on PPISN/PISN models are studied. Various characteristics and results from several PPISN/PISN sim-

ulations are studied using a screening model in which the weak screening factor has been replaced with one developed using the Poisson equation shown in Equation 2.

## 2. Methods

### 2.1. Computational Model

We have used the MESA code (Paxton et al. 2011b) v.11123 to model the collapse and SN explosions of PPISN and PISN respectively. Here, we follow the computations of Marchant et al. (2019). While we summarize the calculation briefly here, we refer to the original paper for details (Marchant et al. 2019). While it is noted that differences exist in various models and computations, we adopt this model for a consistent comparison between the two screening formulations. In this model, we treat stellar evolution beginning with He cores, assuming the H envelope has since been ejected by the wind (Leung et al. 2019). We concentrate primarily on non-rotating models with a metallicity,  $Z = Z_{\odot}/10$ , where  $Z_{\odot} = 0.0142$ . Aside from changing the screening, nearly all of the parameters used here are kept the same as in Marchant et al. (2019). This includes the assumption of hydrostatic equilibrium in early phases of the evolution, with the HLLC solver (Toro et al. 1994) used when the weighted adiabatic exponent  $\langle \Gamma_1 \rangle < (4/3 + 0.01)$  and the central temperature exceeds  $10^9$  K. Additionally, a somewhat higher Fe core infall limit of  $8 \times 10^8$  cm s<sup>-1</sup> was used to avoid interrupting collapse from the pair-instability.

The `approx21` network was used at the onset of the pulsational phase. Some uncertainties have been associated with the use of this network (Marchant et al. 2019), particularly for more massive stars (e.g.,  $M \sim 200 M_{\odot}$ ). However, at lower masses within the PPISN region, the uncertainties in this choice of network have been found to be relatively small.

There are three possible results of this model for the He core progenitors studied. One possibility is a direct collapse in which the Fe core velocity exceeds the infall limit without undergoing a pulse, forming a black hole (BH). Here, we adopt the enclosed baryonic mass prior to direct core collapse as a measure of the resultant black-hole gravitational mass (Fryer 1999), although we note that the BH gravitational mass can be significantly less than the baryonic mass. We also note that recent studies have indicated that a slightly larger mass may result even for massive cores due to fallback in subsequent explosions (Chan et al. 2018; Kuroda et al. 2018). This is expected to occur for lower-mass models with  $M \lesssim 45 M_{\odot}$  and very high mass models with  $M \gtrsim 240 M_{\odot}$  (Farmer et al. 2019).

For intermediate masses with  $45 \lesssim M/M_{\odot} \lesssim 90$ , the star is expected to undergo a PPISN, in which it ejects a possibly significant amount of mass in the wind and pulses before finally collapsing into a BH. The number of pulses that the progenitor undergoes varies with each model, and we study here the dependence on the screening model.

For progenitors with  $90 \lesssim M/M_{\odot} \lesssim 240$ , the star explodes in a PISN, determined by the velocity of each mass element in the model exceeding the stellar escape velocity.

For all of these outcomes, we examine the resultant BH mass, the time to final outcome, the pulse morphology, and the resultant nucleosynthesis - particularly the composition of the ejected mass.

## 2.2. Screening Model

The screening model described in Famiano et al. (2016) was used to determine an effective Debye screening length at high temperatures, and the SEF was calculated in the Salpeter approximation. A specialized screening subroutine was written and adapted into MESA and implemented with an appropriate inlist. For weak screening, two screening modes were explored. The ‘extended’ screening mode implemented in existing versions of MESA and based upon the formulation of Graboske et al. (1973) was used as a default model for comparison. The new ‘relativistic’ mode incorporated the intermediate and strong extended screening modes while replacing the weak SEF with the relativistic factor. Here, the screened reaction rate,  $\Gamma_{scr}$ , between two nuclei of charge  $Z_1$  and  $Z_2$  is enhanced over the unscreened rate,  $\Gamma_0$ , according to:

$$\Gamma_{scr} = \Gamma_0 e^{H_w} , \quad (3)$$

where the weak screening exponent varies between the two models. For extended screening, the weak screening exponent is defined in the literature (Dewitt et al. 1973; Alastuey & Jancovici 1978; Itoh et al. 1979). For both relativistic screening, the exponent is defined using the Salpeter approximation:

$$H_w \equiv \frac{Z_1 Z_2 e^2}{\lambda T} , \quad (4)$$

where  $\lambda$  is the Debye screening length derived in each model. The screening length must also include that of the background ions,  $\lambda_I$  so the total screening length is:

$$\frac{1}{\lambda} = \left[ \frac{1}{\lambda_I^2} + \frac{1}{\lambda_e^2} \right]^{1/2} . \quad (5)$$

For the classical electron screening length, the total Debye length can be shown to match that of Dewitt et al. (1973), which is currently used in the MESA extended screening model.

The electron Debye length is computed for two different regimes characterized by the environmental temperature. At high temperatures,  $kT \sim m_e$ , relativistic effects become more significant. At lower temperatures,  $kT \lesssim m_e$ , a classical approximation is sufficient. Thus, two different approximations for the screening length are used. For  $kT < 150$  keV, the non-relativistic regime is assumed, and MESA’s default classical screening length, which corresponds to the Salpeter screening length (Salpeter 1954) is adopted. For  $kT > 150$  keV, a relativistic approximation of the Thomas-Fermi screening length, described below, is used. In the following we discuss the accuracy of this approximation compared to the numerically computed Thomas-Fermi length. We also highlight the

agreement between the different means to describe screening enhancement factors at the boundary between the relativistic and classical regimes.

We develop a new application of the electron screening length in which relativistic effects from a hot plasma are accounted for. This is distinguished from the commonly used screening length extracted from the linear approximation of the Poisson-Boltzmann equation. For temperatures that are high-enough, pair production can change the total free charges in the plasma, resulting in enhanced screening. At lower temperatures, the classical screening length suffices. We thus define the screening length used in this paper as:

$$\lambda_e = \begin{cases} \lambda_c & \text{for } T < 150 \text{ keV} \\ \lambda_r & \text{for } T \geq 150 \text{ keV} \end{cases} \quad (6)$$

where the usual classical screening length is defined as:

$$\lambda_c \equiv \left[ \frac{T}{4\pi e^2 Y_e \rho N_A} \right]^{1/2} \quad (7)$$

and the relativistic electron screening length is described in a compact form below.

The relativistic electron screening length,  $\lambda_r$ , can be derived following Famiano et al. (2016). For computational speed, we utilize the following approximation:

$$\frac{1}{\lambda_r^2} \approx \frac{4e^2}{\pi} T^2 A [1 - f] \quad (8)$$

where

$$A \equiv \tilde{\mu}^2 + \frac{\pi^2}{3} > 3.28 \quad (9)$$

$$f \equiv \frac{\tilde{m}^2}{2A} - \frac{\tilde{m}^3}{12A} \frac{1}{\cosh^2 \tilde{\mu}/2}$$

where terms expressed with a tilde are divided by the temperature,  $\tilde{X} \equiv X/T$ .

In the weak screening regime, the screening coefficient is given by Equation 4. For strong screening, the same evaluation was used in both models. In this case, the evaluation of Alastuey & Jancovici (1978) was used with plasma parameters from Itoh et al. (1979). This is the default strong screening treatment for the MESA ‘extended’ screening model. For intermediate screening, the screening coefficient in Equation 3 is replaced by an interpolation between the weak and strong screening coefficients as prescribed by the MESA default screening scheme in which the intermediate screening is a weighted sum of the strong and weak screening coefficients,  $H_s$  and  $H_w$ . The weighting factor  $H$  is an average given by the relative difference between the effective screening parameter  $\Gamma_{eff}$  and the boundaries between the strong and intermediate plus intermediate and weak



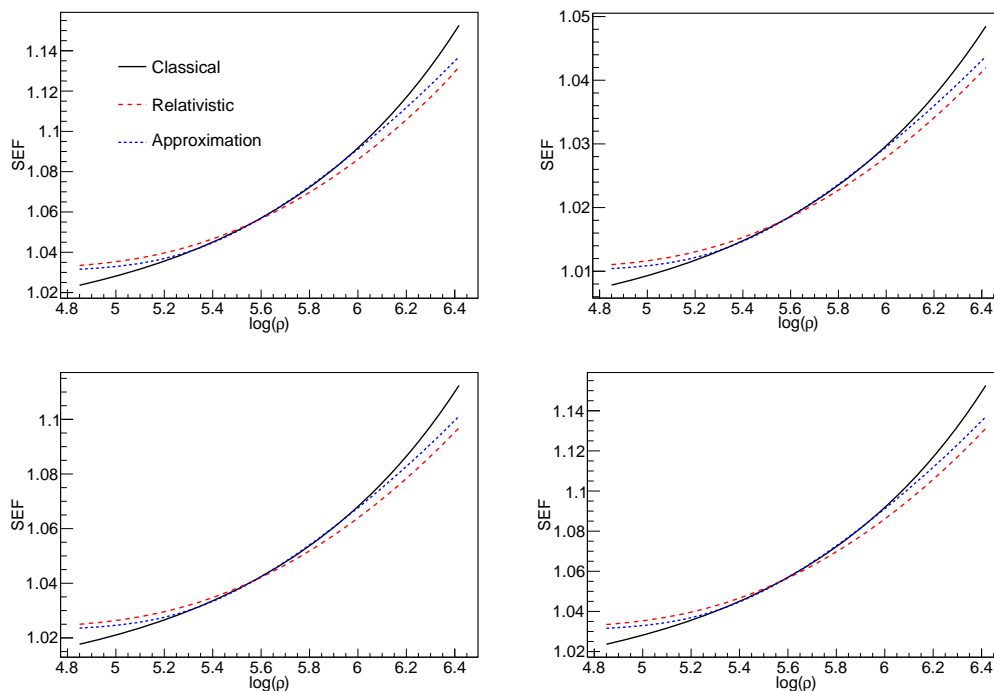


**Fig. 1.** Screening enhancement factors for four major reactant pairs as a function of density at  $kT=150$  keV and  $Y_e=0.5$ . The density at which all SEFs are equal is temperature dependent. (Top left:  $^{12}\text{C}+\alpha$ , Top right:  $^{16}\text{O}+\alpha$ , Bottom left:  $^{12}\text{C}+^{12}\text{C}$ , Bottom right:  $^{16}\text{O}+^{16}\text{O}$ .)

screening regimes:

$$H = H_w \left( \frac{\Gamma_s - \Gamma_{eff}}{\Gamma_s - \Gamma_w} \right) + H_s \left( \frac{\Gamma_{eff} - \Gamma_w}{\Gamma_s - \Gamma_w} \right) \quad (10)$$

$$\Gamma_s > 0.8$$

$$\Gamma_w < 0.3$$

Where the effective screening parameter,  $\Gamma_{eff}$ , is adapted from Alastuey & Jancovici (1978) in Wallace et al. (1982).

Thus, the modification to the MESA extended screening scheme is to replace the weak screening coefficient,  $H_w$ , in Equation 3 and 10 with that of Equation 4 utilizing the relativistic screening length of Equation 8. Further, we restrict this scheme to temperatures above  $kT = 150$  keV ( $T_9 \equiv 1.74$ ). For temperatures below  $kT = 150$  keV, the classical screening length was used. This has been found to be a reasonable demarcation because the difference between the relativistic and the classical SEFs is small at lower temperatures (Famiano et al. 2020). This is shown in Figure 1, in which the SEFs for classical screening, relativistic screening, and the relativistic approximation are shown for various major reactions as a function of density at  $kT=150$  keV. A density range of  $4.8 < \log(\rho) < 6.4$  is shown. This is chosen because for all models, the density when  $kT=150$  keV falls within this range. It can be seen that the SEFs at this temperature are relatively low, compared to SEFs at higher  $T$  or  $\rho$ , and that the numerical relativistic, the relativistic approximation, and the classical screening lengths only vary by  $\sim 1\%$ . This also provides a limitation at very high density to prevent  $k$  from becoming less than zero in the approximation of Equation 8.

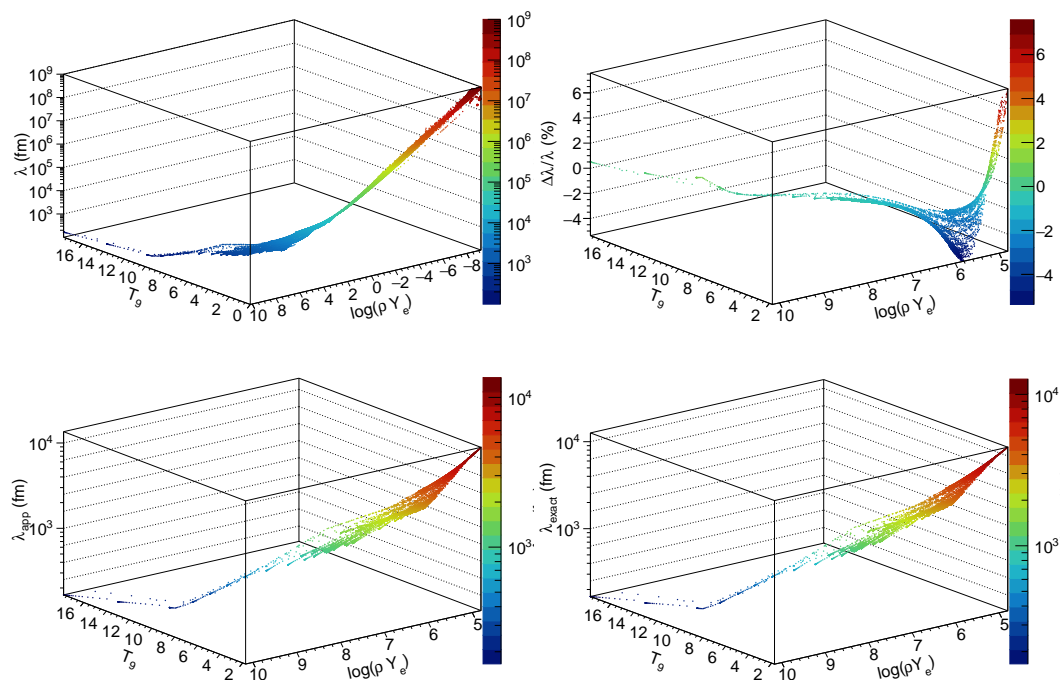


**Fig. 2.** Evaluation of the error and applicability of various screening lengths for a  $70 M_{\odot}$  He core progenitor. Each point in the figures corresponds to an individual mass-time coordinate in the overall evolution of this model from the start of the simulation to the final collapse. (*top left*) Calculated screening length for the entire evolution of the star. The transition from relativistic screening to classical screening occurs at a temperature of 150 keV. The points mesh seamlessly here. (*top right*) The relative uncertainty between the approximation of Equation 8 and the exact numerically calculated screening length. (*bottom left*) The screening length computed using the approximation of Equation 8 for  $kT > 150$  keV. (*bottom right*) The exact numerically calculated screening length for  $kT > 150$  keV.

While computationally efficient, there is some uncertainty in this approximation at low temperatures and high densities.

The  $T = 150$  keV boundary between the use of the classical screening length and the relativistic screening length is somewhat arbitrary. Also, we explore the magnitude of the error induced by using the approximation and the agreement between the classical and the relativistic screening lengths at the boundary. In particular, any uncertainty must be evaluated for the astrophysical site to which it is applicable. Because we are evaluating screening effects in PPISN and PISN, we have explored the errors induced for all the trajectories calculated in a MESA simulation of representative PPISNs and PISNs.

As a representative case, we present calculations of the screening length for temperatures and densities within a  $70 M_{\odot}$  He core progenitor in Figure 2. Here  $T - \rho Y_e$  coordinates are presented for the evolution of this progenitor. Every point in this figure corresponds to a unique mass-time coordinate in the evolution of the star for zones in which the screening length is applicable ( $\Gamma_{eff} < 0.8$  Wallace et al. (1982)). Figure 2 (*top left*) shows the screening length at all points in the evolution. it can be seen that the screening lengths match seamlessly at  $kT = 150$  keV, where the boundary between relativistic and classical screening is set.

The relative error induced in the use of the approximation is shown for all points in the evolution where relativistic screening is used in Figure 2 (*top right*). While the error at low temperatures and

densities is  $\sim 5\%$  or less, the errors at higher temperatures is quite small. This is important to note as the effects of relativistic screening are expected to be more pronounced at higher temperature.

For completeness, the relativistic screening length evaluations are shown in the bottom row of Figure 2. These compare the adopted approximation (*bottom left*) and the exact numerical computation (*bottom right*). These evaluations are shown for all points in the evolution for which  $T > 150$  keV. These figures appear nearly identical.

The same evaluation was done for all models explored in this work, and the errors induced in using the approximation were found to be nearly the same and quite tolerable in every case.

The uncertainty in this evaluation is further explored in Figure 3, where the relative difference in the numerically evaluated screening length,  $\lambda_r$  and the approximation of Equation 8,  $\lambda_{exp}$ , is shown as a function of temperature and density times electron fraction,  $\rho Y_e$ . In the left panel of this figure the relative error of the approximation is shown where  $\Delta\lambda_r \equiv \lambda_{exp} - \lambda_r$ . There is some deviation at the lowest temperatures and densities, where the screening length is small. Also, at low temperatures and very high densities, the uncertainty is larger. However, this temperature-density combination does not occur in any of the simulations presented here as seen in Figure 2 and can thus be ignored in this model. Further, this region is more likely to be in the strong-screening regime, where weak screening is invalid in any evaluation, including the commonly used Salpeter approximation.

The uncertainty is explored further in the right panel of Figure 3, which shows the error in the relativistic screening length as a function of stellar mass and time coordinate for a  $70 M_\odot$  He core progenitor. (For Figures 3 and 4, only the electron screening lengths  $\lambda_e$  are compared for clarity.) In this figure, the time coordinate is the logarithm of the time before final collapse, and the mass coordinate is measured from the center of the star. Each dot in the figure represents a mass-time point in the evolution. The clustering around pulses near  $\log(t_{coll} - t) \approx 2$  and at  $\log(t_{coll} - t) \approx -2$  correspond to small time steps as the temperature gradients are steep for the pulses. Here, only coordinates for which relativistic weak or intermediate screening is relevant (i.e.,  $\Gamma_{eff} < 0.8$  and  $kT > 150$  keV) are displayed as these are the only coordinates for which the relativistic weak screening length is employed. Thus, while it appears that the mass-time points extend above the range of the plot, they actually do not. This is because only the relativistic approximation is being evaluated in this figure. The apparent cutoff in points at the top of the plot is the region where the temperature of the mass zones drops below 150 keV (farther from the stellar core). Beyond these points,  $kT < 150$  keV, so that the default Salpeter screening length is used. These correspond to the central portions of the star as it heats up; one sees that the maximum mass coordinate is  $20 M_\odot$  even though there are cooler mass coordinates in the outer layers of the star. The outer layers of the star are not sufficiently hot for a relativistic treatment. As the central and outer layers of the star get hotter, the mass coordinates for which relativistic screening becomes relevant increases towards the outer edge of the remnant. It is seen that the error in the screening length is within 10% of the true value for all time and mass elements in this treatment.

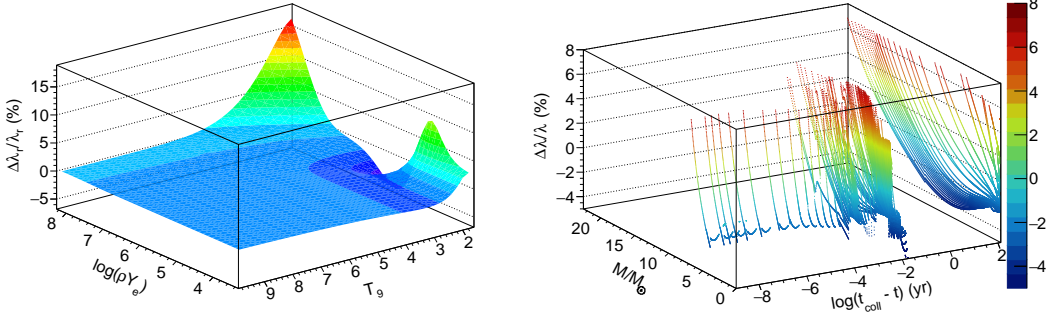


**Fig. 3.** (left) Relative error in relativistic Debye length using the approximation of Equation 8. (right) Relative error in relativistic Debye length for individual zones in the MESA evolution for a  $70 M_{\odot}$  He progenitor as a function of time prior to collapse. Each dot in the figure is a mass element at a specific time step. Only times at which  $T > 150$  keV and mass elements for which weak or intermediate relativistic screening is appropriate are shown.

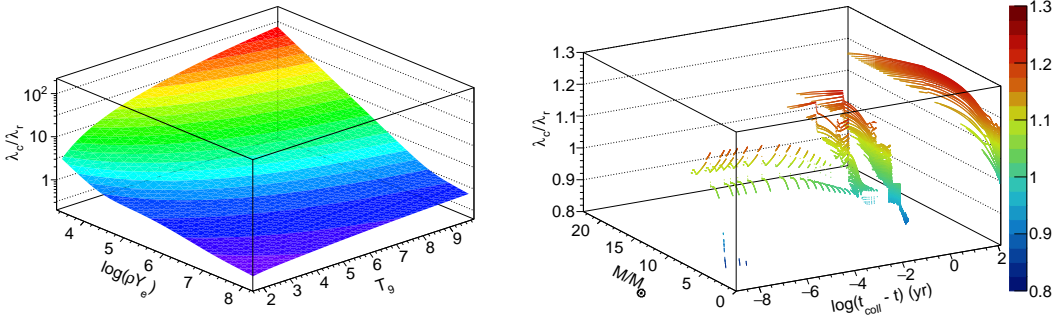


**Fig. 4.** (left) Ratio of classical to relativistic electron screening lengths for the weak and intermediate screening as a function of temperature and electron density. (right) Ratio of classical to electron screening lengths for a  $70 M_{\odot}$  model evolution. The time is shown as time before final collapse. Each dot is a mass element and a time step. In the figure, values less than unity are blue, while those greater than unity are green.

The relative difference between the classical and relativistic Debye lengths  $(\lambda_c - \lambda_r)/\lambda_c$  for the same site is shown in Figure 4. In the left panel, the ratio of the classical to the relativistic Debye length is shown as a function of  $\rho Y_e$  and temperature,  $T_9$ . It is seen that the classical Debye length is larger than the relativistic Debye length for most of the area of this plot, except at low temperatures and higher densities, where the classical Debye length is smaller than the relativistic Debye length. We note that, at constant density, the classical Debye length increases monotonically with temperature, while the relativistic Debye length decreases. In typical astrophysical conditions, the points where  $\lambda_c < \lambda_r$  are in the strong screening regime, and weak screening is not relevant anyway. This is shown in the right panel for the same mass-time elements as in Figure 3. This shows that the early pulses (that are closer to the surface where the density is lower) have a shorter  $\lambda_r$ . Except for a very few high-density points near the core, the relativistic screening length is shorter than the classical screening length. Naively, it is expected that the relativistic Debye screening always results in increased rates, and we can see that this is true overall except for a few very short periods of time in a very small region near the high-density core.

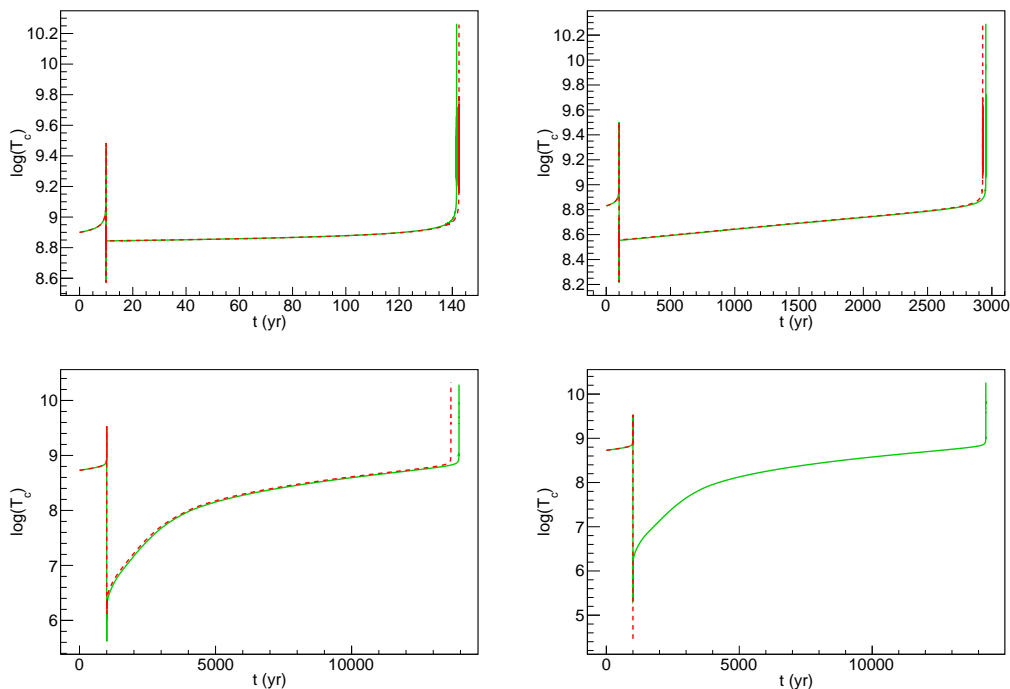


**Fig. 5.** Logarithm of central temperature,  $\log T_c$  versus time for various progenitor models. The solid green lines correspond to the default screening model, and the dashed red lines correspond to the relativistic screening model. (*top left*)  $70 M_\odot$ , (*top right*)  $76 M_\odot$ , (*bottom left*)  $89 M_\odot$ , and (*bottom right*)  $89.02 M_\odot$

### 3. Results

Multiple PPISN and PISN simulations were run varying by the initial mass and metallicity. For the bulk of the simulations, the initial metallicity was set to  $Z = Z_\odot/10$ . We examined ejected mass, final BH mass, pulse morphology, ejection time, and nucleosynthesis in each model. Representative results are presented here.

#### 3.1. Pulsational Time

Time characteristics of the central temperature, which is used to define a pulse (Marchant et al. 2019), are shown for multiple representative progenitors in Figures 5 – 7. Progenitor masses in this figure are chosen to cover the full range of black-hole masses resulting from PPISN as well as progenitors in the region which produces the most massive black holes in the PPISN region.

At the low end of the PPISN mass range, for  $44.5 M_\odot$  progenitors, stars undergo a direct collapse after losing roughly  $10 M_\odot$  to the wind. At low progenitor mass, near the transition between direct collapse to PPISN, the central temperature may exhibit an extended amount of time undergoing “weak pulses” (Woosley 2017) indicated by the oscillations in the central temperature prior to the final collapse. For the direct collapse BH at  $44.5 M_\odot$ , the unstable pulsation for relativistic screening is more prominent. However, these weak pulses do not occur in the default screening model. In this borderline region, the very slightly increased reaction rates at high temperature in the early pulsational stages results in a transition from direct collapse to PPISN at a slightly (negligibly) lower mass. While the instabilities occur at roughly the same time for both the default and

relativistic screening models, the instabilities last for a longer period of time and they extend the collapse to later times at low mass. For the default screening model, the onset of these weak pulses and unstable pulsation occurs at a slightly higher mass in which the core temperature and density undergoes a transition from conditions that result in direct collapse to that of a PPISN.

For masses around  $70 M_{\odot}$ , which will be shown to produce the more massive black holes, the first pulses are found to occur at roughly the same time. This is reasonable given that the core temperatures prior to the pulse do not exceed the threshold for relativistic screening until near the peak of the short time pulse. However, because of the slight differences in burning and composition in both models, subsequent pulses and collapse occur at different times.

For the  $89 M_{\odot}$  model, in which only one full pulse occurs prior to collapse, the final collapse time occurs slightly earlier for relativistic screening. In this model, reaction rates during the first pulse are increased by relativistic screening as the relativistic Debye length is shorter. While the final nucleosynthetic abundances are not changed significantly, the processing is slightly faster.

In the case of the  $80.92 M_{\odot}$  progenitor, the default screening model proceeds to collapse, while the relativistic model proceeds to a PISN. This mass is right at the PPISN/PISN boundary, and the rates for the relativistic model produce a very slight increase in the overall nuclear heating during the first pulse. This region is a high-mass equivalent to the low-mass region at which the star is close to being unstable against collapse or explosion.

Details of the first pulses in several models are shown in Figure 6. For the low-mass models near the boundary between direct collapse and PPISN collapse, the weak pulses can be seen in detail. The mass at which the weak pulses appear is lower in the relativistic model, and the pulsation extends for a longer period of time prior to collapse in the  $45 M_{\odot}$  model. For the intermediate masses near  $70 M_{\odot}$ , there is little difference in the pulse morphology of the first pulses.

For the high-mass progenitors near the PPISN/PISN boundary, it can be seen that the time to restore the star to the quiescent phase takes longer with increasing progenitor mass. In the case of the  $89.02 M_{\odot}$  model, the star can be seen to undergo several oscillations in the central temperature before it stabilizes for the default screening model. However, in the case of relativistic screening, the explosion ends the stellar evolution at the first pulse. The ultimate effect here is to reduce the mass at which the PPISN/PISN boundary occurs. We note, however, that this reduction is very small and within the uncertainties of the current model (Farmer et al. 2019).

In all cases, the evolution up to the first pulse is similar in both screening models. However, the subsequent evolution may be different in terms of the total time to collapse/explosion and in terms of pulse morphology. Figure 7 shows the central temperature evolution for the final pulses in various stellar progenitor models. While the pulse morphology looks similar in all cases, some changes in the number of pulses, pulse distribution and the pulse shape can be observed. For example, in the  $52 M_{\odot}$  relativistic model, the increased rates in the final pulsation results in an additional period of weak pulsation near 303 years. The number of pulses later on are roughly the same, though they

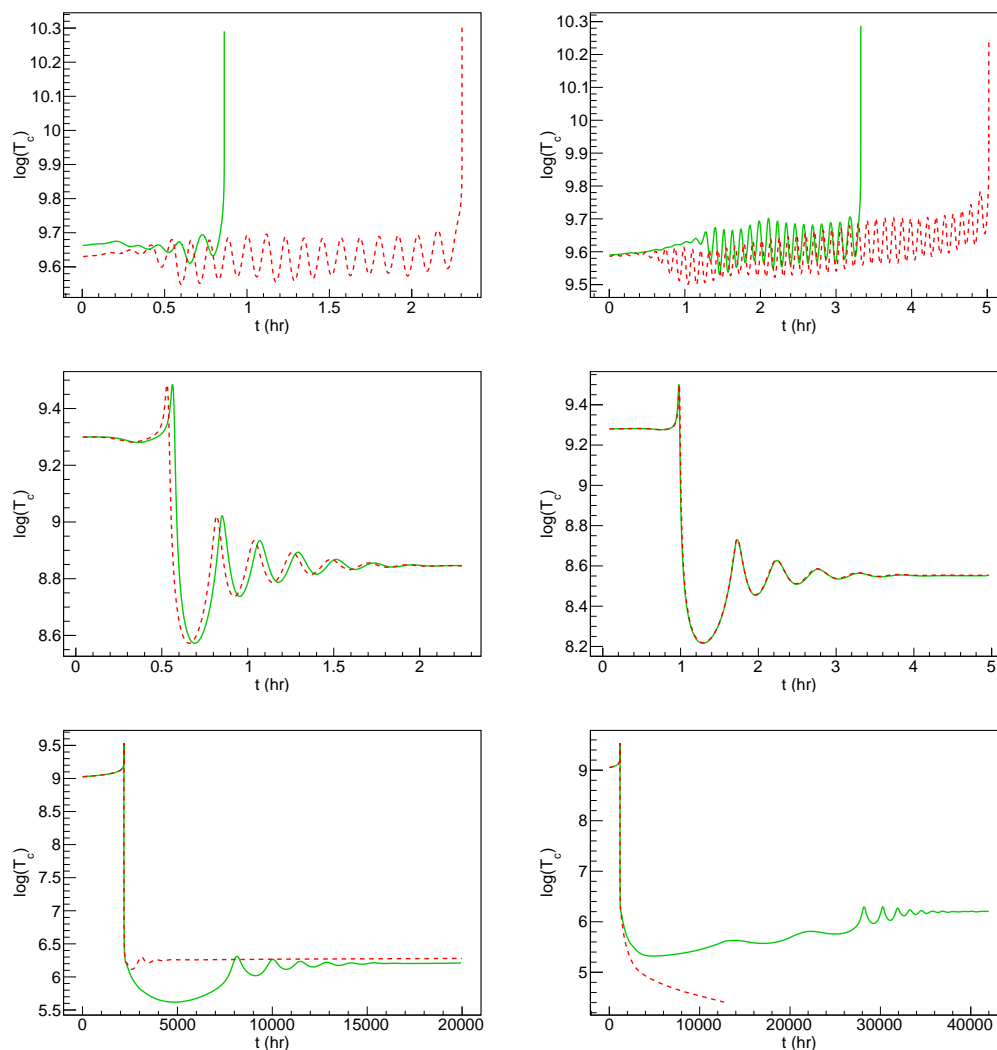


**Fig. 6.** Logarithm of central temperature showing detail of the first pulse for several progenitors. The lines are the same as in Figure 5. (*top left*)  $44.5 M_{\odot}$ , (*top right*)  $45 M_{\odot}$ , (*middle left*)  $70 M_{\odot}$ , (*middle right*)  $76 M_{\odot}$ , (*bottom left*)  $89 M_{\odot}$ , and (*bottom right*)  $89.02 M_{\odot}$ .

occur at different times. Overall, for this mass, the core spends more time at temperatures for which relativistic screening becomes important.

In the case of the  $58 M_{\odot}$  model, the earlier pulse structure in the figure is dramatically different, and the core undergoes fewer pulses at the latest times. Overall, this results in the  $58 M_{\odot}$  relativistic model spending a much smaller amount of time at relativistic temperatures.

In the case of the  $70 M_{\odot}$  model, the pulse morphology is similar in both cases, with the number of pulses and pulse duration similar in the default and relativistic screening cases. The total time to collapse from the initial pulse is only slightly longer in the relativistic model.

The total time from the onset of the initial pulse (defined as the time at which the central temperature first exceeds  $150 \text{ keV}$ ) to final collapse or explosion is shown in Figure 8 (*left*). This figure provides a comparison of the total time spent in the instability region for a PPISN. In this figure, the sharp drop at  $\sim 89 M_{\odot}$  occurs at the boundary between the PPISN and PISN. At this mass boundary, the PISN may undergo a single sharp rise in core temperature followed by an explosion as the

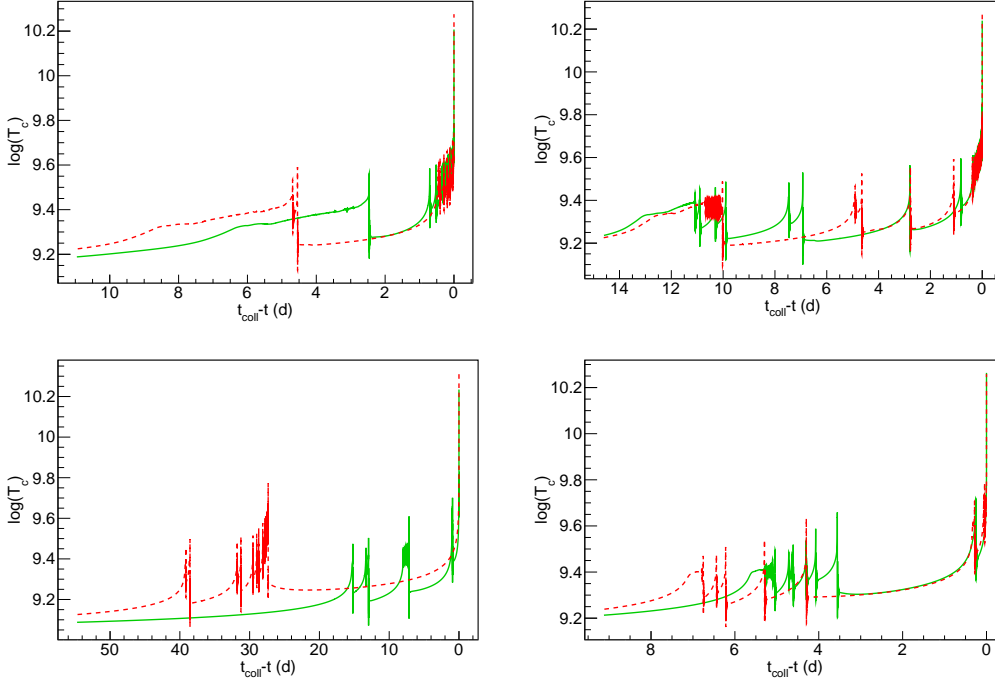


**Fig. 7.** Detail of central temperature for three progenitor models for both default (solid green lines) and relativistic (dashed red lines) screening rates. (*top left*)  $52 M_{\odot}$ , (*top right*)  $58 M_{\odot}$ , (*bottom left*)  $64 M_{\odot}$ , and (*bottom right*)  $70 M_{\odot}$ . The relativistic screening case has been offset by 6.82 yr for the  $52 M_{\odot}$  model and by  $-2.79 \times 10^4$  s for the  $70 M_{\odot}$  model so that both evolution plots can fall within the same range.

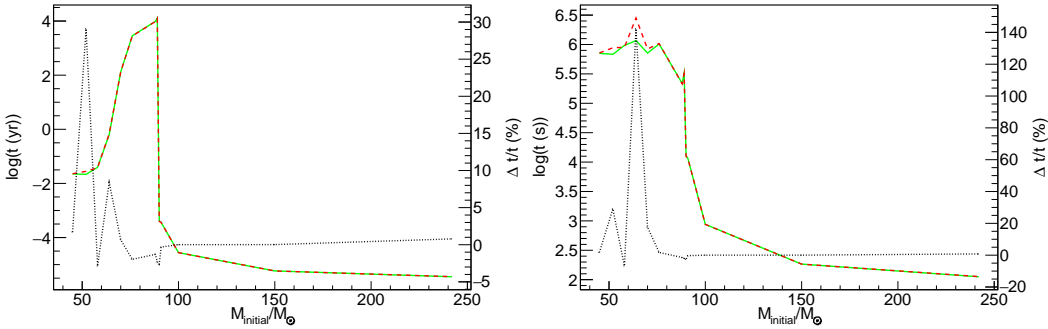


**Fig. 8.** (*left*) Time elapsed between initial pulse and final progenitor collapse or explosion as a function of initial mass. (*right*) Cumulative time for which the core temperature  $kT > 150$  keV as a function of initial mass. The solid green lines correspond to extended screening calculations. The red dashed lines correspond to relativistic screening calculations. The dotted black lines are the relative time difference between relativistic screening and default screening.

entire star expands faster than the local escape velocity. At the low-mass end of the PPISN region, the total time to collapse is also small as the star undergoes only a single pulse. For intermediate masses ( $45 M_{\odot} < M < 89 M_{\odot}$ ), additional pulses increase the time to collapse, though the time between the first and second pulses tends to dominate the evolution in this model (Marchant et al. 2019).

In the intermediate mass region, the evolution is not only dominated by the number of pulses, but also the pulse morphology and stellar heating. For example, for a  $52 M_{\odot}$  star, the additional pulsation shown in Figure 7 creates an extended period during which relativistic screening is promi-



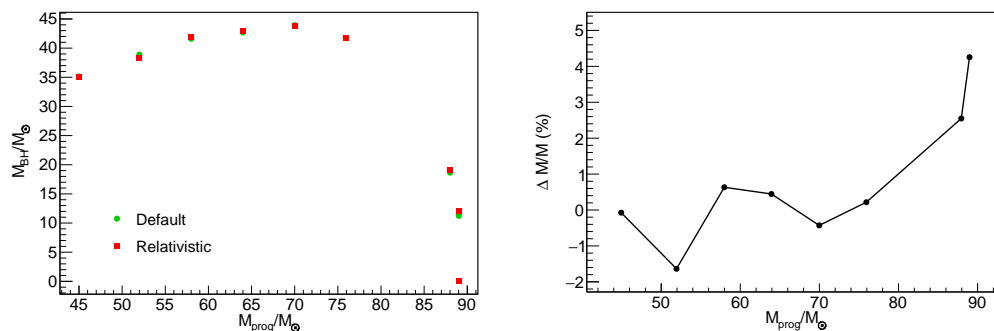


**Fig. 9.** (*left*) Resultant BH mass versus He core progenitor mass for models including the extended screening and relativistic screening. The PPISN-PISN cutoff lies between  $89.02M_{\odot}$  and  $89.05M_{\odot}$  for the default screening model and between  $89M_{\odot}$  and  $89.02M_{\odot}$  for the relativistic screening model. (*right*) Relative shift in the resultant BH mass when relativistic screening is used compared to the default screening model.

ment. This can affect the nucleosynthesis and mass ejection during the pulse, which will be discussed later.

Perhaps a better metric for evaluating the impact of relativistic effects is the total time at which the star’s core temperature exceeds 150 keV. This is important as it provides a metric for mass models for which the largest differences may be expected. This is shown in Figure 8 (*right*). Because of the instability of the PPISN progenitors, there can be dramatic deviations over the entire mass range. For example, for a  $58 M_{\odot}$  progenitor, the number of pulses and pulse time vary little between the first and last pulse, resulting in little difference in times spent at high temperature in each model. For the  $52 M_{\odot}$  progenitor, the additional instability and pulsation just prior to collapse results in significantly more time spent at high temperature. The same is true for the  $64 M_{\odot}$  model, in which the extended instability and the additional time to collapse result in a significantly longer time spent at high temperature, where relativistic effects could be more prominent. The much longer time for the  $64 M_{\odot}$  model is shown as the large spike in the relative time difference in Figure 8 (*right*).

### 3.2. Black Hole Masses for PPISN

For PPISN, with progenitor core masses  $44.5 \leq M/M_{\odot} \leq 89$ , the final BH mass was determined in both the default and relativistic screening models. As stated previously, the final baryonic mass is adopted as a reasonable measure of the BH gravitational mass (Fryer 1999). The final BH mass as a function of progenitor mass is shown in Figure 9 (*left*). The difference in masses between both models as a function of progenitor mass is shown in Figure 9 (*right*) where  $\Delta M/M \equiv (M_{BH,rel} - M_{BH,def})/M \times 100\%$ . In either case it is seen that the influence of relativistic screening is negligibly small as the change in mass is likely smaller than the numerical uncertainties of the model (Farmer et al. 2019). The BH masses shown in Figure 9 (*left*) are in the mass range  $11.22 < M_{BH}/M_{\odot} < 43.94$ . These values are comparable to those extracted from recent LIGO/VIRGO data for binary-black-hole merger events (Abbott et al. 2019). Lighter BH merger events, such as GW170608 contained lower-mass black holes which likely originated from core-collapse supernova events and not PPISNe. One merger event, GW170729, was found to contain a  $50.2 M_{\odot}$  BH, which lies in

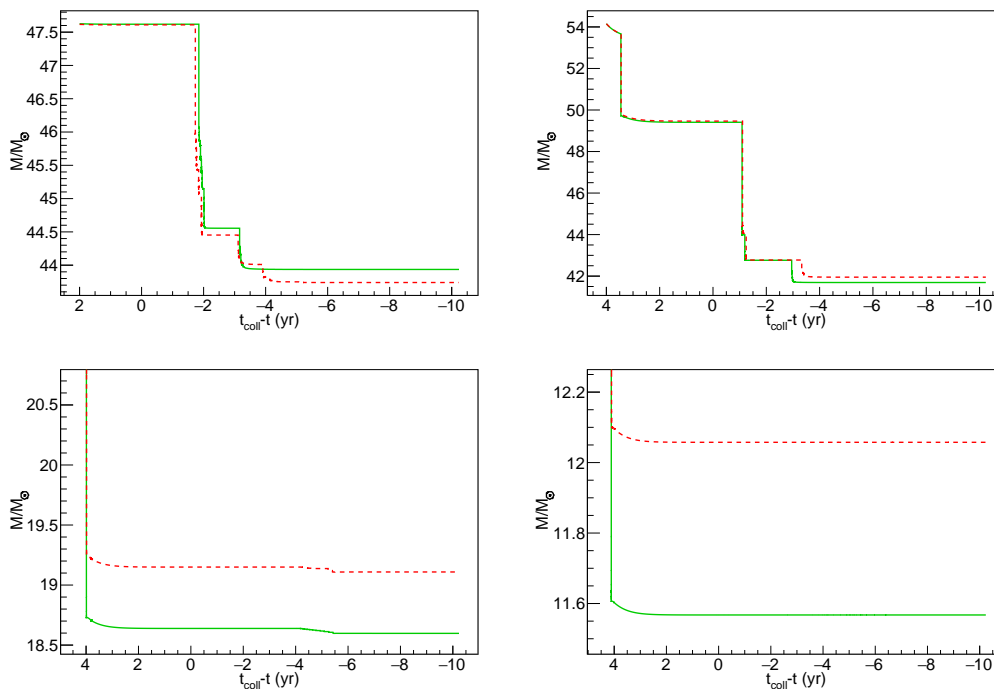


**Fig. 10.** Stellar mass as a function of time. Evolution is tracked as the logarithm of the time before final collapse and is shown after the first pulse. Shown is the mass below the escape velocity. The solid green line is for the default screening model, while the dashed red line is for the relativistic screening model. (*top left*)  $70 M_{\odot}$ , (*top right*)  $76 M_{\odot}$ , (*bottom left*)  $88 M_{\odot}$ , and (*bottom right*)  $89 M_{\odot}$ .

the mass gap in which massive stars are thought to undergo PISN. It has been found, however, that these more massive BHs may be formed if the  $^{12}\text{C}(\alpha,\gamma)^{16}\text{O}$  lower, while still being within the 68% confidence interval for this rate (Farmer et al. 2019).

A significant portion of the mass loss in each case comes from the individual pulses themselves, with most of the pulsational mass loss from the first pulse. Much of the He loss is from the wind prior to the first pulse. This can be seen in Figure 10, which shows the mass loss for various progenitors at the first pulse and up to the time of collapse. Shown in this figure is the total stellar mass below the stellar escape velocity as a function of time for various progenitor masses. In each case, a significant amount of mass loss occurs during the first pulse. While subsequent pulses occur, the mass loss may not be as pronounced. However, the  $76 M_{\odot}$  progenitor shows significant mass loss during subsequent pulses. Also observable is the difference in the stellar mass for each model. A larger resultant BH for the most massive PPISN, while the final BH for a  $70 M_{\odot}$  model is smaller. It is also noted that relativistic effects shift the PPISN/PISN boundary to lower progenitor mass. However, this shift is insignificant.

### 3.3. Nucleosynthesis of PISN

Figures 11 and 12 show the total ejected mass of isotopes as a function of the progenitor mass. The ejected mass includes mass ejected in the wind and in the individual pulses. Also shown in this

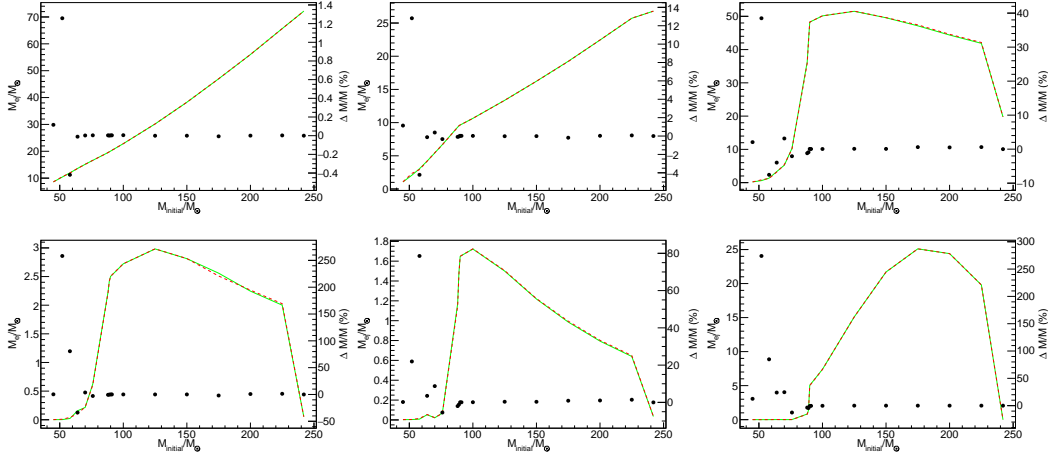


**Fig. 11.** Cumulative ejected mass of various isotopes as a function of the initial mass for nuclei up to and including  $^{28}\text{Si}$ . The solid green line corresponds to models using extended screening, while the dashed lines correspond to models using relativistic screening. The dots are the relative difference in ejected mass between relativistic and extended screening computations. (top left)  $^4\text{He}$ , (top middle)  $^{12}\text{C}$ , (top right)  $^{16}\text{O}$ , (bottom left)  $^{20}\text{Ne}$ , (bottom middle)  $^{24}\text{Mg}$ , and (bottom right)  $^{28}\text{Si}$ .

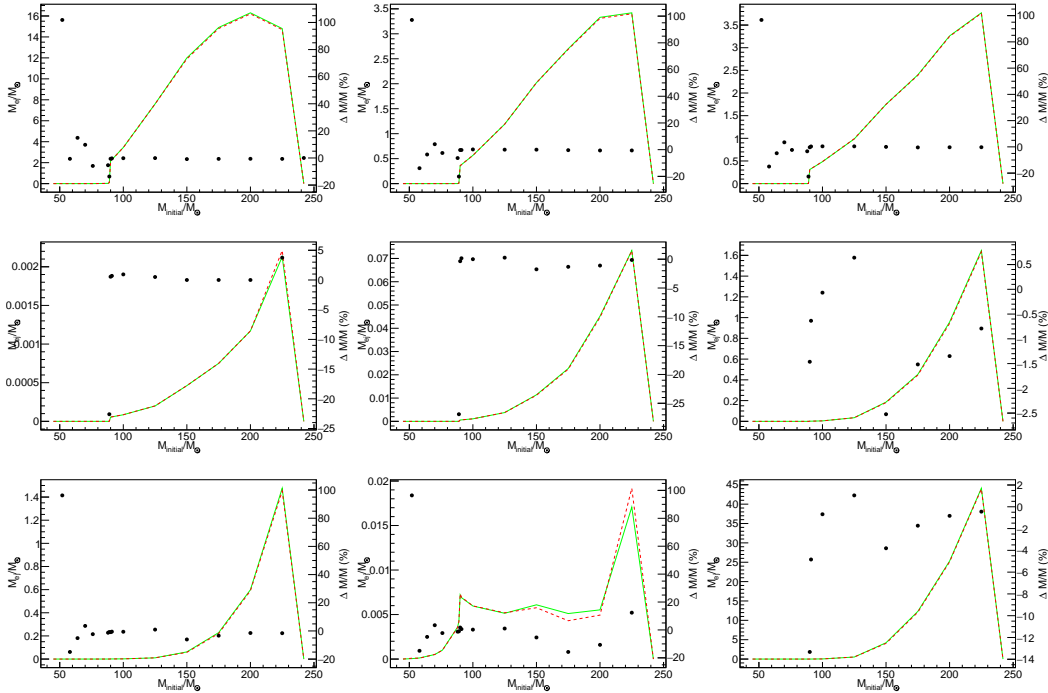


**Fig. 12.** Same as Figure 11 except for nuclei heavier than  $^{28}\text{Si}$ . (top left)  $^{32}\text{S}$ , (top middle)  $^{36}\text{Ar}$ , (top right)  $^{40}\text{Ca}$ , (middle left)  $^{44}\text{Ti}$ , (center)  $^{48}\text{Cr}$ , (middle right)  $^{52}\text{Fe}$ , (bottom left)  $^{54}\text{Fe}$ , (bottom middle)  $^{56}\text{Fe}$ , and (bottom right)  $^{56}\text{Ni}$ .

figure is the relative difference of mass ejected between each model:

$$\frac{\Delta M}{M} \equiv \frac{M_{ej,rel} - M_{ej,ext}}{M_{ej,ext}}. \quad (11)$$

In the case of  $^4\text{He}$ , the difference in both models is not found to be significant. Nearly all of the  $^4\text{He}$  is ejected in the wind for all progenitors. For nuclei heavier than  $^4\text{He}$ , the ejected mass is significantly affected by the subsequent pulsations of the star.

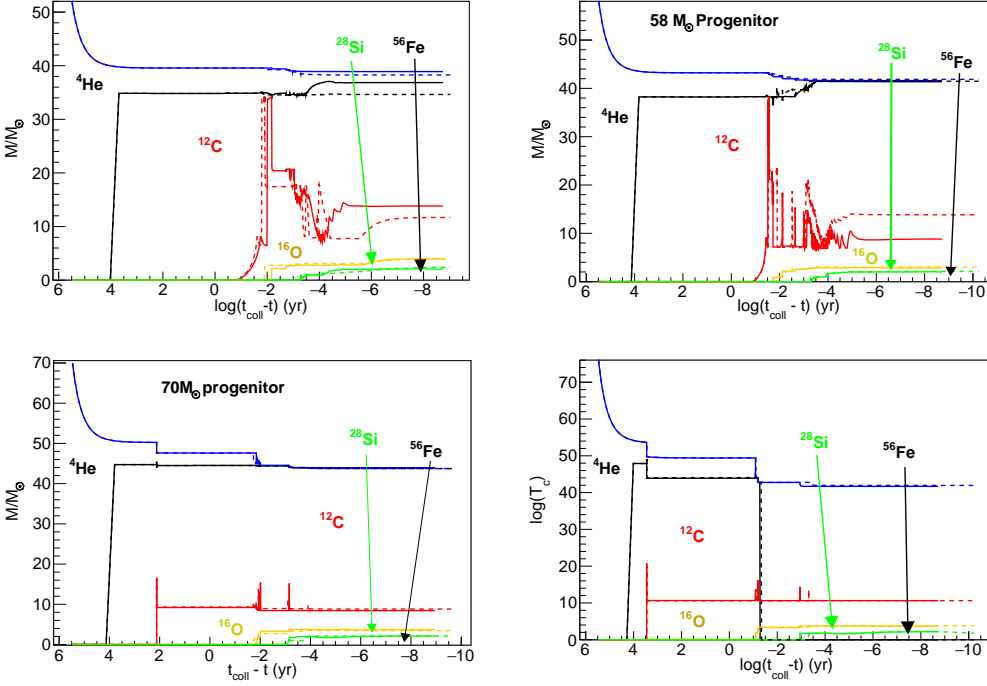


**Fig. 13.** Kippenhahn diagram comparison for four progenitors. Lines indicate the mass element at which the mass fraction of the indicated isotope falls below  $10^{-2}$ . The mass of each layer is indicated, along with the total mass of the star below the escape velocity. Dashed lines are for the relativistic model and solid lines are for the default screening model. Convective and burning regions have been removed for clarity. (*top left*)  $52 M_{\odot}$ , (*top right*)  $58 M_{\odot}$ , (*bottom left*)  $70 M_{\odot}$ , and (*bottom right*)  $76 M_{\odot}$ .

For many of the models, it would appear that the amount of mass ejected in the relativistic model is largest relative to the amount of mass ejected in the extended model for a progenitor mass of  $\sim 52 M_{\odot}$ . This is probably because this progenitor undergoes the largest number of pulses, and more importantly, spends more time at a central temperature where relativistic effects are important. Here, it might not be surprising that burning will progress more rapidly to produce more species heavier than  $^{12}\text{C}$  at the stellar surface for progenitors which undergo more pulses. For progenitors with masses between  $70$  and  $76 M_{\odot}$ , there are several pulses, and the mass ejected per pulse is larger. This results in a larger amount of mass ejected as shown in Figures 11 and 12 but increased burning beyond  $^{24}\text{Mg}$  results in a depletion of the lighter nuclei for higher-mass progenitors.

For nuclei heavier than  $^{24}\text{Mg}$ , very little mass is ejected unless the evolution results in a PISN, ejecting all of the mass in the star. Because much of the mass of these nuclei is confined to the core, and because the individual pulses preceding a PPISN primarily eject surface layers, the heavy nuclei are maintained in the core of the star as it collapses into a BH. This is seen in the figure as a sharp increase in the ejected mass of  $^{28}\text{Si}$  and heavier for  $\sim 90 M_{\odot}$ . At a mass roughly equal to the PPISN/PISN cutoff, there is a sharp increase in the relative difference in ejected mass. This difference is particularly visible for the heavier nuclei and to a lesser extent for the lighter nuclei. This sharp increase corresponds to the very narrow range of progenitor mass which results in a PISN for the relativistic model, but a PPISN in the extended model. For progenitors heavier than this cutoff in both models, the ratios are very close to zero as all of the stellar mass is ejected

into the ISM after a very short increase in core temperature. Much of the production of heavier nuclei in stars undergoing PISNe is from hydrostatic burning at lower temperature.

For the Fe in the PISN region ( $M_{initial} \sim 150 M_{\odot}$ ), the relativistic model ejects slightly less Fe than the extended model. However, only a very small amount of Fe is ejected in either model, and the difference is small. For direct collapse, progenitors with  $M \geq 242 M_{\odot}$  eject no Fe as the star undergoes a direct collapse into a BH, and only lighter-mass nuclei are ejected in the wind prior to collapse.

In fact, it is seen that for the massive stars that undergo PISNe or direct collapse, there is little or no difference in the ejecta for all nuclei. This is because the stellar interior either does not reach a core temperature hot enough for relativistic screening to be significant, or the core temperature is hot for a very short period of time.

The progenitors in the mass region between 50 and 64  $M_{\odot}$  are particularly interesting with regard to the production of nuclei less massive than  $^{24}\text{Mg}$ . Here the dynamics and interplay between the number of pulses, core temperature, surface ejecta, and the wind can be quite complicated. Relativistic screening for the 52  $M_{\odot}$  model results in an increase in the ejection of lighter nuclei, with the largest enhancement for  $^{20}\text{Ne}$  (although it is important to note that only a very small amount of  $^{20}\text{Ne}$  is ejected by the 52  $M_{\odot}$  model). However, for the 58  $M_{\odot}$  model, there is a smaller amount of He, C, and O ejected for relativistic screening. This may be due to the enhanced burning of these nuclei as the star progresses to the production of more massive nuclei.

Figure 13 shows Kippenhahn diagrams for four representative models. Shown are the mass lines as a function of  $\log(t_{coll} - t)$  where  $t_{coll}$  is the final collapse time. Each line in these diagrams corresponds to the location at which the mass fraction of the labeled isotope falls below  $10^{-2}$ . Also shown is the total stellar mass below the escape velocity. (Convective and burning zones are not shown for simplicity.) In the case of the 52  $M_{\odot}$  and 58  $M_{\odot}$  models, there is a significant convection zone after the first pulse starting at the boundary of the C/O layer. This is likely responsible for the rapidly changing behavior between these two models. In the relativistic model, the C layer extends to deeper in the star prior to collapse for the 52  $M_{\odot}$  model, while it does not extend as deeply as that for the default screening formulation in the 58  $M_{\odot}$  model. It can be seen in Figure 11 that more C is ejected in the 52  $M_{\odot}$  model if relativistic effects are considered, but less is ejected for the 58  $M_{\odot}$  model. Similar results are seen for O.

This emphasizes the complexity of nucleosynthesis within the PPISN model and the changes in rates between these two formulations of electron screening. Because the screening correction is density-dependent, rates in the relativistic screening model do not always exceed those of the default screening model. Furthermore, the pulse number, duration, shape, and quiescent period all vary between these formulations. While fewer pulses are expected to result in a lower ejected mass, a longer pulsational period (including weak pulses) can have the opposite effect.

## 4. Conclusions

A screening model was developed for MESA in which electron-positron charge density and distribution were treated in an environment in which pair-production is possible. Existing routines have been adapted to incorporate a new screening type for all MESA simulations.

As a first test of this model, relativistic screening for pulsational pair-instability supernovae and pair instability supernovae (PPISNe and PISNe) has been explored. Comparisons were made to prior models over a range of masses including low-mass He core progenitor stars, which undergo direct BH collapse; stars which undergo direct collapse after one or more thermal pulses; stars which explode in PISNe as every mass element exceeds the local escape velocity; and massive stars which undergo direct collapse.

The inclusion of relativistic screening was found to change the overall pulsational morphology and timing characteristics of the pulsational phase of the star. This is not surprising as relativistic screening is most prominent at higher temperatures. The pulsational phase of the star was found to achieve temperatures in the core and elsewhere of well over 150 keV, the cutoff temperature for relativistic screening. For masses near  $44.5 M_{\odot}$ , the unstable temperature oscillations were found to extend for a longer period of time prior to the final collapse of the star. It was also found that the PPISN/PISN boundary occurs at lower mass. However, the shift in this boundary with mass insignificant in light of the other uncertainties in this model.

Because of the unstable nature of the pulsational phase of PPISNe, slight changes in the reaction rates and heating due to small changes in screening can result in changes in the timing characteristics of the pulses. A notable case is the  $64 M_{\odot}$  model, for which the heating is more pronounced in the month prior to collapse. For other models, shifts in pulses, the appearance of weak pulses, and changes in the overall timing of the final pulses can result from the inclusion of relativistic screening.

The changes induced in the temperature characteristics of the pulsational phase can also affect the resulting nucleosynthesis slightly. Here, we examined the composition of material ejected in the winds and pulses. For stars that undergo total destruction in a PISN, little change was found in the composition of ejected mass between the default and the relativistic model. However, for resulting PPISNe, there could be changes in the total masses of ejected isotopic species as the total surface composition could vary with each model. For nuclei less massive than  $^{28}\text{Si}$ , differences in the ejected mass of specific species could exceed 200%. However, the total mass of light nuclei ejected by PPISNe is generally small. This reflects the effects of the steep mass profile within the star and how small differences in mass profiles at the surface can result in large relative changes in the total ejecta of one specie. For progenitors with masses  $70 < M/M_{\odot} < 90$ , where mass loss from pulsation becomes significant, the ejected mass of light nuclei increases. In this region, the relative differences in the ejected mass of a particular specie is generally less than 10%.

For lighter progenitors, with  $M < 70 M_{\odot}$ , the ejected mass can be quite small,  $\sim 5 M_{\odot}$  or less for C and O. However the differences in the mass ejected can be more significant. It is as much

as 40%(14%) for O(C) ejected by a 52  $M_{\odot}$  star. Differences in the convection induced by heating differences in each model are also noted, as shown in Figure 13.

The maximum BH mass formed in this study, which is produced by a  $\sim 70 M_{\odot}$  He core, was found to vary little by the addition of relativistic screening. At higher progenitor masses, the resultant BH mass was found to increase by roughly 0.5  $M_{\odot}$ . However, this increase is probably negligible given the uncertainties of the model used. Though the changes in rates induced by a relativistic treatment of screening change the BH mass only slightly, the resultant composition of the ejecta, being sensitive to the surface composition, was found to vary somewhat for lighter progenitors and lighter stars. While this may not significantly change models for late time galactic chemical evolution, it may be worth exploring the effects of changes in the galactic chemical evolution of the early galaxy from the possible nucleosynthesis in Pop III stars which undergo PPISNe.

*Acknowledgements.* T.K. is supported in part by Grants-in-Aid for Scientific Research of JSPS (17K05459, 20K03958). A.B.B. is supported in part by the U.S. National Science Foundation Grants No. PHY-2020275 and PHY-2108339. M.A.F. is supported by National Science Foundation Grant No. PHY-1712832 and by NASA Grant No. 80NSSC20K0498. K.M. is supported by Research Institute of Stellar Explosive Phenomena at Fukuoka University. M.A.F., G.J.M. and A.B.B. acknowledge support from the NAOJ Visiting Professor program. Work at the University of Notre Dame (G.J.M.) supported by DOE nuclear theory grant DE-FG02-95-ER40934.

## References

- Abbott, B. P., Abbott, R., Abbott, T. D., et al. 2019, *Physical Review X*, 9, 031040
- Abbott, R., Abbott, T. D., Abraham, S., et al. 2020, *Phys. Rev. Lett.*, 125, 101102
- Abbott, R., Abbott, T. D., Abraham, S., et al. 2020, *The Astrophysical Journal*, 900, L13
- Adelberger, E. G., Austin, S. M., Bahcall, J. N., et al. 1998, *Reviews of Modern Physics*, 70, 1265
- Alastuey, A. & Jancovici, B. 1978, *ApJ*, 226, 1034
- Belczynski, K., Heger, A., Gladysz, W., et al. 2016, *A&A*, 594, A97
- Boyd, R. N. 2008, *An Introduction to Nuclear Astrophysics* (The University of Chicago Press (London))
- Chan, C., Müller, B., Heger, A., Pakmor, R., & Springel, V. 2018, *ApJ*, 852, L19
- Clayton, D. D. 1983, *Principles of Stellar Evolution and Nucleosynthesis* (The University of Chicago Press (Chicago)), 357 – 359
- Croon, D., McDermott, S. D., & Sakstein, J. 2020, *Phys. Rev. D*, 102, 115024
- Dewitt, H. E., Graboske, H. C., & Cooper, M. S. 1973, *ApJ*, 181, 439
- Famiano, M., Balantekin, A. B., Kajino, T., et al. 2020, *ApJ*, 898, 163
- Famiano, M. A., Balantekin, A. B., & Kajino, T. 2016, *Phys. Rev. C*, 93, 045804
- Farmer, R., Renzo, M., de Mink, S. E., Marchant, P., & Justham, S. 2019, *ApJ*, 887, 53
- Fryer, C. L. 1999, *ApJ*, 522, 413
- Graboske, H. C., Dewitt, H. E., Grossman, A. S., & Cooper, M. S. 1973, *ApJ*, 181, 457
- Heger, A. & Woosley, S. E. 2002, *ApJ*, 567, 532
- Ichimaru, S. 1993, *Reviews of Modern Physics*, 65, 255
- Iliadis, C. 2007, *Nuclear Physics of Stars* (WILEY-VCH Verlag GmbH & Co. (Weinheim))
- Itoh, N., Hayashi, H., Nishikawa, A., & Kohyama, Y. 1996, *ApJS*, 102, 411
- Itoh, N., Totsuji, H., & Ichimaru, S. 1977, *ApJ*, 218, 477
- Itoh, N., Totsuji, H., Ichimaru, S., & Dewitt, H. E. 1979, *ApJ*, 234, 1079
- Jancovici, B. 1977, *Journal of Statistical Physics*, 17, 357
- Kapusta, J. I. & Gale, C. 2006, *Finite-Temperature Field Theory: Principles and Applications* (Cambridge University Press (Cambridge))
- Kozyreva, A., Gilmer, M., Hirschi, R., et al. 2017, *MNRAS*, 464, 2854

- Kravchuk, P. A. & Yakovlev, D. G. 2014a, *Phys. Rev. C*, 89, 015802
- Kravchuk, P. A. & Yakovlev, D. G. 2014b, *Phys. Rev. C*, 89, 015802
- Kuroda, T., Kotake, K., Takiwaki, T., & Thielemann, F.-K. 2018, *MNRAS*, 477, L80
- Leung, S.-C., Nomoto, K., & Blinnikov, S. 2019, *ApJ*, 887, 72
- Liu, J.-J. 2016, *Research in Astronomy and Astrophysics*, 16, 83
- Marchant, P., Renzo, M., Farmer, R., et al. 2019, *ApJ*, 882, 36
- Meyer, B. S. & Adams, D. C. 2007, *Meteoritics and Planetary Science Supplement*, 42, 5215
- Paxton, B., Bildsten, L., Dotter, A., et al. 2011a, *ApJS*, 192, 3
- Paxton, B., Bildsten, L., Dotter, A., et al. 2011b, *ApJS*, 192, 3
- Paxton, B., Marchant, P., Schwab, J., et al. 2015, *ApJS*, 220, 15
- Paxton, B., Schwab, J., Bauer, E. B., et al. 2018, *ApJS*, 234, 34
- Potekhin, A. Y. & Chabrier, G. 2013, *Contributions to Plasma Physics*, 53, 397
- Quarati, P. & Scarfone, A. M. 2007, *ApJ*, 666, 1303
- Sahoo, B. K. & Das, M. 2016, *European Physical Journal D*, 70, 270
- Sakstein, J., Croon, D., McDermott, S. D., Straight, M. C., & Baxter, E. J. 2020, *Phys. Rev. Lett.*, 125, 261105
- Salpeter, E. E. 1954, *Australian Journal of Physics*, 7, 373
- Salpeter, E. E. & van Horn, H. M. 1969, *ApJ*, 155, 183
- Shalybkov, D. A. & Yakovlev, D. G. 1987, *Astrophysics*, 27, 562
- Shaviv, G. & Shaviv, N. J. 2000, *ApJ*, 529, 1054
- Spera, M. & Mapelli, M. 2017, *MNRAS*, 470, 4739
- Spitaleri, C., Bertulani, C., Fortunato, L., & Vitturi, A. 2016, *Physics Letters B*, 755, 275
- Takahashi, K., Yoshida, T., & Umeda, H. 2018, *ApJ*, 857, 111
- Toro, E. F., Spruce, M., & Speares, W. 1994, *Shock Waves*, 4, 25
- van Son, L. A. C., De Mink, S. E., Broekgaarden, F. S., et al. 2020, *ApJ*, 897, 100
- Wallace, R. K., Woosley, S. E., & Weaver, T. A. 1982, *Ap. J.*, 258, 696
- Wang, B., Bertulani, C. A., & Balantekin, A. B. 2011, *Phys. Rev. C*, 83, 018801
- Woosley, S. E. 2017, *ApJ*, 836, 244
- Woosley, S. E. 2019, *ApJ*, 878, 49
- Woosley, S. E., Blinnikov, S., & Heger, A. 2007, *Nature*, 450, 390
- Woosley, S. E. & Heger, A. 2021, *ApJ*, 912, L31
- Wu, Y. & Pálffy, A. 2017, *ApJ*, 838, 55